analytical chemistry

Article

Ferroelectric Perovskite Oxide@TiO2 Nanorods Heterostructures: Preparation, Characterization and Application as Platform for Photoelectrochemical Bioanalysis

Li-Min Yu, Yuan-Cheng Zhu, Yi-Li Liu, Peng Qu, Mao-Tian Xu, Qi Shen, and Wei-Wei Zhao

Anal. Chem., **Just Accepted Manuscript** • DOI: 10.1021/acs.analchem.8b01820 • Publication Date (Web): 21 Aug 2018

ACS Publications

is published by the American Chemical Society. 1155 Sixteenth Street N.W., Washington, DC 20036

Ferroelectric Perovskite Oxide@TiO_2 Nanorods Heterostructures: Preparation, Characterization and Application as Platform for Photoelectrochemical Bioanalysis

Li-Min Yu,[a,b,c,e] Yuan-Cheng Zhu,[b,e] Yi-Li Liu,[a,b,c,e] Peng Qu,*[a,c] Mao-Tian Xu,[a,c] Qi Shen,[c] Wei-Wei Zhao*[b,d]

[a]Henan Key Laboratory of Biomolecular Recognition and Sensing, College of Chemistry and Chemical Engineering, Shangqiu Normal University, Shangqiu 476000, China

[b]State Key Laboratory of Analytical Chemistry for Life Science, School of Chemistry and Chemical Engineering, Nanjing University, Nanjing 210023, China

[c]College of Chemistry and Molecular Engineering, Zhengzhou University, Zhengzhou 450001, China

[d]Department of Materials Science and Engineering, Stanford University, Stanford, California 94305, United States

[e]These authors (L.-M. Y., Y.-C. Z. and Y.-L. L) contributed to this work equally.

* E-mail: qupeng0212@163.com * E-mail: zww@nju.edu.cn; zww@stanford.edu

ABSTRACT: This work reports the first synthesis and characterization of ferroelectric perovskite oxide-based heterostructure as well as its application for photoelectrochemical (PEC) bioanalytical purpose. Specifically, exemplified by the $[KNbO_3]_{1-x}[BaNi_{1/2}Nb_{1/2}O_{3-\delta}]_x$ (KBNNO), the ferroelectric perovskite oxides were prepared by the solid-state synthesis, while the TiO_2 nanorods (NRs) arrays were obtained via the hydrothermal method. Using the technique of pulsed laser deposition (PLD), the KBNNO were then deposit on the TiO_2 NRs to form the KBNNO@TiO_2 NRs heterostructures. Various characterization techniques were applied to reveal the compositional and structural information of the as-fabricated sample and favorable alignment existed between the two components as displayed by the PEC test. In the detection of L-Cysteine, the as-fabricated KBNNO@TiO_2 NRs demonstrated good performance in terms of sensitivity and selectivity. This work unveiled the promise of ferroelectric perovskite oxide and its based heterostructures for innovative PEC bioanalytical application and we hope it could inspire more interests in the development of various ferroelectrics-based heterostructures for advanced PEC bioanalysis.

Photoelectrochemical (PEC) bioanalysis, a rapidly evolving technique for advanced biomolecular detection, generally necessitates appropriate photoelectrodes as sensing platforms to accommodate the particular probes and recognition events.[1-6] Since the inception of this technique, analysts have been infatuated with developing unique photoelectrodes for innovative applications.[7-14] Ideal candidates should support efficient light harvesting, proper biomolecule interfacing, enhanced and stable photocurrent generation, fast responsibility as well as sensitive signal transduction when implemented in a bioanalytical system.[15-21] To this end, previous efforts have exploited diverse photoactive materials, mainly including various inorganic nanomaterials and organic semiconductors, such as CdS/CdTe quantum dots (QDs),[14, 22-24] TiO_2 nanomaterials[13, 25] and porphyrin as well as its derivatives.[26] Recently, advanced hierarchical heterostructures have experienced soaring popularity due to their combined properties and desirable performance.[27-30] Well alignment of different components could contribute to the exciton generation/transfer and thus result in better photoelectrodes with favorite characteristics. In this respect, for example, graphitic carbon nitride sensitized with CdS QDs has been applied for PEC aptasensing of tetracycline.[31] CdTe-graphene oxide (GO) was used in a dual channel self-reference PEC biosensor.[8] Core-Shell $NaYF_4$:Yb,Tm@TiO_2 upconversion microrods was studied for a near-infrared-to-ultraviolet light-mediated PEC aptasensing.[32] Previously, we have also proposed a plasmonic scheme consisting of Au nanoparticles (NPs) and a Sillen-Aurivillius perovskite of Bi_4NbO_8Cl.[33]

Ferroelectrics, which enable a spontaneous electric polarization that can be reversed by an external electric field, have ignited tremendous interest as a candidate family of materials for photovoltaic and related light-energy-harvesting applications.[34-36] For example, , an interesting perovskite ferroelectric solid-solution, $[KNbO_3]_{1-x}[BaNi_{1/2}Nb_{1/2}O_{3-\delta}]_x$ (KBNNO), has recently been developed with tunable direct bandgap (1.1-3.8 eV) matching the solar spectrum, rendering it suitable for the visible light absorption (1.39 eV) and many conversion utilizations.[37-43] Given their fascinating potentials, surprisingly, hardly any work about these materials has been explored in the field of PEC bioanalysis. We assume that the ferroelectrics family could provide a unique opportunity to construct an innovative hierarchical heterostructure as exquisite PEC platform. Unfortunately, such a possibility has not been unveiled.

With this motivation and exemplified by KBNNO, this scenario describes the first synthesis and characterization of the ferroelectrics@TiO_2 nanorods (NRs) arrayed heterojunction as well as its application as new PEC bioanalytical platform.

Specifically, as shown in Scheme 1a, the solid-solution of KBNNO with various composition ratio were prepared by the solid-state synthesis and then sintered as KBNNO target, while the TiO_2 NRs arrays were obtained via the hydrothermal method. Subsequently, with the aid of pulsed laser deposition (PLD) technique, the condensed KBNNO target were directed to deposit onto the TiO_2 NRs for the first time. The X-ray diffraction (XRD), scanning electron microscope (SEM), transmission electron microscope (TEM), X-ray photoelectron spectroscopy (XPS) and Raman analysis et al. were applied to reveal the compositional and structural information of the sample and PEC characterization displayed its excellent light absorption property. Subsequently, as displayed in Scheme 1b, this heterostructure was appied to the the PEC detection of L-cysteine (Cys), an essential sulfur-containing amino acid, which was served as an effective electron donor in present system. The as-fabricated KBNNO@TiO_2 NRs demonstrated good performance in terms of sensitivity and selectivity. This work features the exploration of ferroelectric perovskite oxide and its based heterostructures for PEC bioanalysis, which to our knowledge has not been reported. This work manifested their attractive potential in future PEC bioanalysis, and we expect it could inspire more interest in the development of various ferroelectrics-based heterostructures for advanced PEC bioanalysis.

Scheme 1. Schematic Illustrations for (a) the Preparation of KBNNO@TiO_2 NRs Heterostructures and (b) Its Application for PEC Bioanalysis of Cys

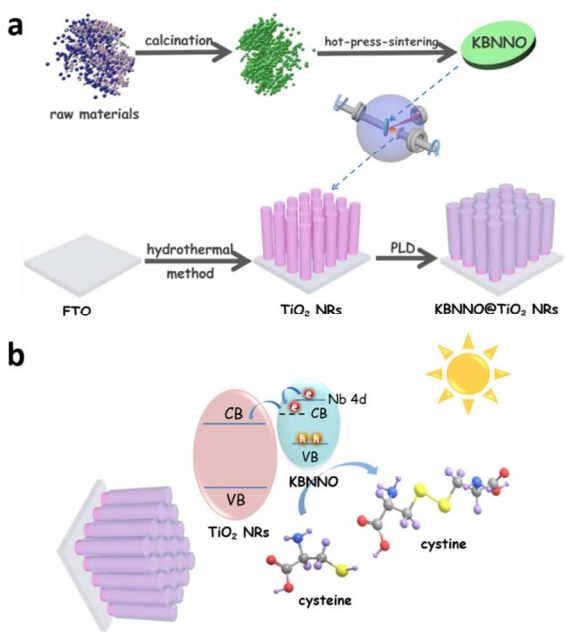

EXPERIMENTAL SECTION

Reagents and Apparatus. Potassium Carbonate (K_2CO_3), Barium Carbonate ($BaCO_3$), Niobium Pentaoxide (Nb_2O_5), Nickel Oxide (NiO) were supplied from Sinopharm Chemical Reagent Co., Ltd (China). Titanium tetrachloride ($TiCl_4$) was perchased from Tianjin Kermel Chemical Reagent Co., Ltd. Hydrochloric acid (HCl, 36.5%-38% by weight) was supplied from Xilong Chemical Reagent Co., Ltd. The Fluorine-doped tin oxide (FTO) glass (14 ohm per square) was obtained from Wuhan Geao science and education instrument Co., Ltd. Bovine serum albumin (BSA), L-Glutathione reduced (GSH), uric acid (UA), dopamine (DA), ascorbic acid (AA) and Homocystine (Hcy) were purchased from Sigma-Aldrich (St. Louis, MO). Cys, glucose (Glu), β-lactose (Lac), L-lysine (Lys), lactic acid (Lac), sarcosine (Sar), tryptophan (Try) and urea were purchased from Nanjing Chemical Reagent Co., Ltd. (Nanjing, China). Phosphate buffer solution (PBS, pH 7.4) was prepared from $Na_2HPO_4 \cdot 12H_2O$ (Nanjing Chemical Reagent Co., Ltd., 99.0%) and NaH_2PO_4 (Nanjing Chemical Reagent Co., Ltd., 99.0%). Ultrapure water (18.2 MΩ·cm resistivity at 25 °C, Millier Q) was used in all experiments.

SEM images were performed with a JSM-6701F scanning electron microscope (Japan). TEM and HRTEM was recorded by a JEM-1210 microscope (JEOL, Japan). XPS was obtained from ESCALAB 250Xi (Thermo Scientific, Japan). XRD spectra were operated at 40 kV, 150 mA with Cu-Kα radiation (Rigaku D/max-2400, Japan, λ = 0.15418 nm). The Raman scattering spectra was determined by a Czemy-Tumer Labram HR 800 Raman spectroscopy using a laser light wavelength of 532 nm. PEC measurements were performed from a computer controlled electrochemical workstation (CH Instruments, CHI 660d) equipped with a xenon lamp with a power density of 100 mW cm^{-2}. The power density of solar simulator was calibrated with a reference silicon solar cell (CEL-RCCO, China). Photocurrent was measured in an electrochemical cell with a three-electrode system: a KBNNO@TiO_2 NRs electrode as the working electrode, a Pt plate as the counter electrode and a saturated mercury electrode (SCE) as the reference electrode. A 0.05 M Na_2S and 0.95 M Na_2SO_3 solution was used as the supporting electrolyte for photocurrent measurements. All the PEC measurements were operated in atmospheres. For Cys detection, the experiments were processed with a homemade PEC system. The irradiation source is a 5 W LED lamp which can produce the white light in front of the electrode. The electrochemical cell consisted of KBNNO@TiO_2 NRs electrode, a Pt wire counter electrode and an Ag/AgCl reference electrode (with KCl in the saturated solubility) in 0.1 M PBS solution.

Synthesis of KBNNO: The KBNNO power was prepared by conventional standard solid-state synthesis method according to the previous report.[37-38] All components in different ratios were synthesised by stoichiometric quantities of K_2CO_3, $BaCO_3$, Nb_2O_5 and NiO as starting raw materials. The powders were ball-milled media in ethanol with Tungsten carbide (WC) balls for 2 h in Pulverisette 5 Planetary high-energy-mill. The weight ratio of the ball to the powders is 10:1. The milled powders were sieved with 200 mesh sieve after drying at 60 °C for 4 h and calcined in an alumina crucible at 900 °C for 12 h. The KBNNO target was obtained by vacuum hot-pressed sintered technology as follows: the mixture was cold compacted in a graphite die (Φ 61 mm × 6 mm) and hot-sintered under the pressure of 25 MPa with a dynamic vacuum of about 10^{-3} Pa at 850 °C for 2 h in a vacuum hot-pressing furnace (ZT-45-20, ShangHai Chen Hua Electric Furnace Co. Ltd., China). Then, the specimens were machined to remove surface impurities and polished into fixed dimension (Φ 60 mm × 5 mm) for later sputtering application.

Synthesis of TiO_2 NRs: TiO_2 nanorodes (NRs) arrays was fabricated on FTO glass substrate adopting the hydrothermal method that has been reported in detail elsewhere.[44-45] One piece of the FTO glass substrate was firstly ultrasonically cleaned in a mixture of deionized water, 2-propanol and

acetone with volume ratio of 1:1:1 for 60 min, subsequently rinsed extensively with deionized water, then dried with N_2 stream and finally was placed at an certain angle against the wall of Teflon-lined reactor with the conducting side facing down. 40 mL of HCl was mixed with 40 mL deionized water. The mixture was stirred for 5 min before 0.6 mL $TiCl_4$ was added and then poured into Teflon-lined reactor after being stirred for another 5 min. The hydrothermal synthesis was operated at 180 ^oC for 3 h in oven. After synthesis, the hydrothermal synthesis reactor was cooled to room temperature under flowing cold water. Subsequently, the sample was taken out, rinsed with ultrapure water and finally dried in an electric oven at 60 ^oC.

Synthesis of KBNNO@TiO_2 NRs: KBNNO@TiO_2 NRs was fabricated by PLD technique (COMPexPro 205) with a KrF excimer laser (λ_L = 248 nm, pulse duration τ_L= 25 ns (FWHM), repetition rate 5 Hz).[46-47] The KBNNO target was fixed in target holder while the FTO-TiO_2 NRs substrate was fixed in sample supporter. Prior to ablating the KBNNO target, the deposition chamber was evacuated by the coalition of mechanical pump and molecular pump to 2.4 × 10^{-4} Pa. Both the KBNNO target and FTO-TiO_2 NRs substrate were cleaned by oxygen plasma for 5 min before ablating the target in O_2 atmosphere. The target was placed parallel to FTO-TiO_2 NRs substrate with a distance of 55 mm. In the pulse sputtering, parameters were interceded as follows: laser energy was set in 300 mJ and pulse frequence was set as 5 Hz as well as 6000 number of pulses was presented. Futhermore, a speed of 15 rpm of the target rotational speed was applied during the laser ablating for avoiding the deep craters' formation, and the sample supporter ratated at the speed of 10 rpm in order to achieve uniform films.

PEC Detection: Solutions with different concentrations of Cys were prepared before analyzing and then PEC measurements were performed on the assembled electrodes at room temperature. The specificity experiments were then evaluated with different biological analytes including Glu, Lac, GSH, Lys, Lac, Sar, Try and BSA in the electrolyte of 0.1 mol L^{-1} PBS.

RESULTS AND DISCUSSION

Structural and Compositional Characterization. Figure 1 showed the SEM images of as-prepared TiO_2 NRs and KBNNO powders, as well as the corresponding XRD patterns and Raman spectroscopy of KBNNO powders. Figure 1a presented the typical top-view SEM of TiO_2 NRs, which exhibited a self-organized NRs structure with good conformity on the FTO substrate. Figure 1a inset of the cross-sectional image indicates these NRs were approximately 2.67 μm in length and vertically aligned with smooth surface. Obviously, such a well-aligned structure could not only provide large surface area for the following PLD deposition of guest material (KBNNO), but also be advantageous to the increased light absorption and efficient directional charge transportation within the arrayed NRs. The morphology of as-prepared KBNNO powder (x = 0.3) was shown in Figure 1b, which manifested that the particles were spherical with a size of ca. 100 nm, and a lot of particles spliced with each other to form a cohesive body. The EDS mapping in Figure S1 recorded the corresponding elemental distribution of KBNNO powder (x = 0.3). Figure S2 demonstrated the morphologies of as-prepared KBNNO powders with variable component ratio. As shown, the radius of KBNNO (x = 0.1, 0.2, 0.3, 0.4) powders decreased distinctly compared with $KNbO_3$ (KNO, x = 0.0). This phenomenon can be ascribed to the inner lattice strains on account of different ionic radius of Ni/Nb and K/Ba. In addition, Ba^{2+} at A-site leaded to the generation of K^+ vacancies, which reduced growth velocity of crystal and resulted in the decline of particle size ultimately.[48]

XRD patterns of the different KBNNO target components were recorded with the results shown in Figure 1c. The appearance of NiO diffraction peak came from the NiO additive after doping with Ni/Ba elements. All the XRD analysis related KBNNO matched well with the International Centre for Diffraction (ICDD) data: The diffraction peaks for pure KNO could be indexed as the orthorhombic crystal lattice in the space group of Amm2 (JCPDS no. 71-2171), while the patterns of Ni/Ba doped KBNNO material could be fully indexed as cubic perovskite crystal of the Pm3m space group (JCPDS no. 52-1517). Furthermore, it can be evidently noticed that peaks of (211) and (112) have been merged into one single peak for KBNNO compositions according to the enlargenment of area marked with gray bar, which was magnified in Figure 1d. Therefore, it can be inferred that the composition in the KBNNO underwent a wide phase evolution: i.e., from orthorhombic lattice to tetragonal system and tetragonal system to cubic phase. Besides, the diffraction patterns of KBNNO gradually shifted to lower diffraction angels with the increasing Ni/Ba content, which was mainly due to the introduction of larger ionic radius Ni^{2+} (0.69 Å) based on the Bragg equation.

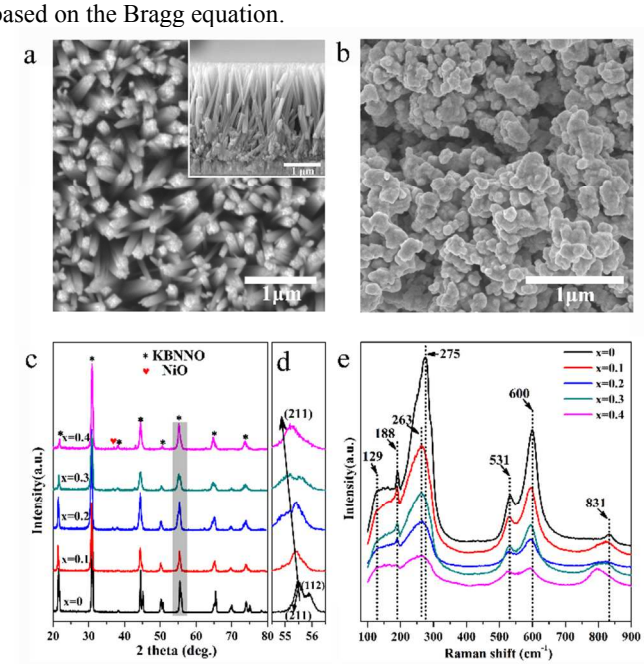

Figure 1. (a) Top-view FESEM of TiO_2 NRs. Inset: the corresponding cross-sectional view. (b) The SEM image of KBNNO nanoparticles (x = 0.3). (c) XRD patterns of the as-prepared KBNNO (x = 0, 0.1, 0.2, 0.3, 0.4) targets, respectively. (d) XRD peaks of the enlargenment of area marked with gray bar in Figure 1c. (e) Raman spectroscopy of the different KBNNO components (x = 0, 0.1, 0.2, 0.3, 0.4).

Raman spectroscopy, a competent examination method to analyze the phase evolution and stucture change, was then applied to investigate the as-synthesised KBNNO samples on account of its sensitivity to small distortions of crystal lattice. Figure 1e depicted the Raman spectra data of $KNbO_3$ and

Ni/Ba-doped KBNNO samples. The band at 129 cm^{-1} can be assigned to A-O (K-O or Ba-O) vibrations, suggesting the existence of K^+ and Ba^{2+} cations. The peaks at 188 cm^{-1} and 275 cm^{-1} can belong to a frigerprint for the long-range polar order,[49] and their sharp dip demonstated that the long-range polar order weaken languishingly with the increase of Ni/Ba content. Furthermore, the peaks for pure $KNbO_3$ appeared at 275 cm^{-1} can be assigned to Nb-O_6 bending mode and 531 cm^{-1} and 600 cm^{-1} can be ascribed to Nb-O_6 stretching mode, while peaks located at 263 cm^{-1} for KBNNO shifted to a lower wavenumber by 12 cm^{-1}. The reason was that the O-Ni-O vibration had substituted part of O-Nb-O vibration, indicating the successful Ni-doping in KBNNO. Normally, a lower Raman stretching frequency implied a longer length of the metal-oxygen bond. The Raman data shift towarded left, especially at the band of 600 cm^{-1} and 831 cm^{-1}, signified the significantly increasment of O-Ni-O bond, which was corresponding to the pattern of XRD.

Using the PLD technique, the KBNNO were then deposited onto the TiO_2 NRs to form the as-designed KBNNO@TiO_2 NRs heterostructures. Figure 2a showed the cross-sectional SEM image of the as-synthesized KBNNO@TiO_2 NRs arrays (x = 0.3). It is clear that the KBNNO@TiO_2 NRs kept similar morphology to that of TiO_2 NRs after sputtering KBNNO, indicating the covering of KBNNO on the TiO_2 surface will not affect their NRs shape. TEM was then used to disclose more structural information about KBNNO@TiO_2 NRs. Figure 2b presented the TEM image of a truncated single KBNNO@TiO_2 NR, which possessed a rough surface which might be caused by the KBNNO deposition. The HRTEM image in Figure 2c demonstrated that the TiO_2 NRs was covered by an irregular granule KBNNO film of ca. 2.66 nm. However, the KBNNO film was in amorphous structure, while the TiO_2 NRs are of its single-crystalline nature. Besides, no interspace can be seen, indicating the strong contacts between TiO_2 NRs and KBNNO shell. To further validate the formation of KBNNO@TiO_2 NRs, elemental mapping was performed with the results shown in Figure 2d. Obviously, each element has been detected by the energy dispersive X-ray spectroscopy (EDS), the homogenous distrubution of these elements verified the successful deposition of KBNNO shell onto TiO_2 NRs. XPS was further utilized to determine the surface chemical compositions and valence states of the as-fabricated KBNNO@TiO_2 NRs, with the binding energy of contaminated carbon (C 1s = 284.8 eV) as the internal marked standard. Figure 2e depicted the survey spectrum of the sample with the relevant elements of Ni, O, K, Ba and Nb, while the corresponding high-resolution XPS spectra of Ni 2p and Ba 3d were illustrated in Figure 2f. Ni 2p signal located at about 855.08 eV can be assigned to the unreacted NiO and the peak at 856.49 eV was ascribed to the Ni atom in KBNNO crystal, which confirmed the substitution of Ni^{2+} with Nb^{5+} in the Ni-doped KBNNO system. As shown in Figure 2f inset, the Ba 3d peaks located at 794.57 eV and 779.19 eV with a peak separation of 15.38 eV.

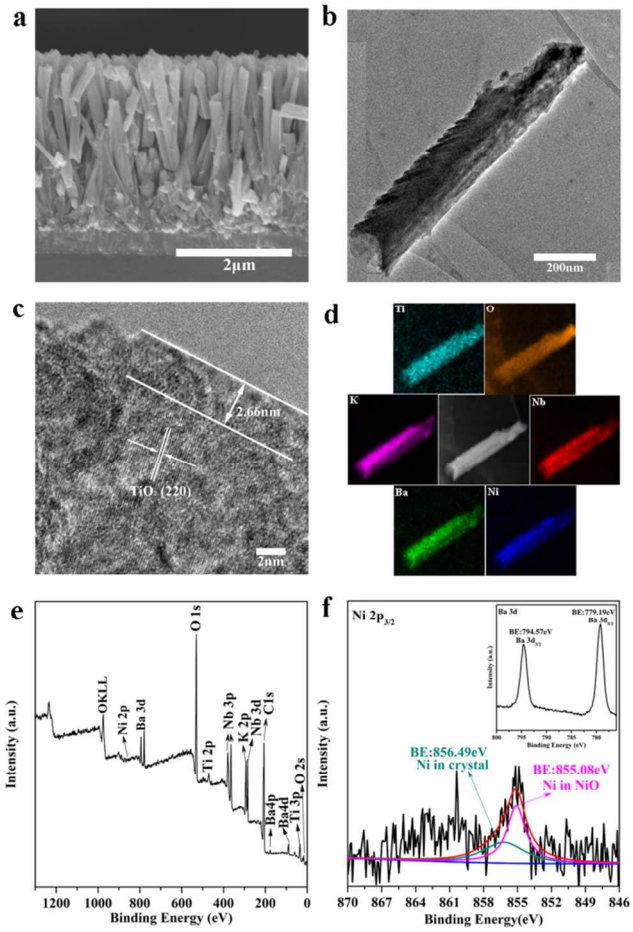

Figure 2. (a) The cross-sectional SEM of the as-prepared KBNNO@TiO_2 NRs (x = 0.3). (b) TEM image of single KBNNO@TiO_2 NR (x = 0.3). (c) The HRTEM image of KBNNO@TiO_2 NR. (d) The EDS mapping of single KBNNO@TiO_2 nanorod (x = 0.3). (e) The full-scan XPS spectrum of the as-fabricated KBNNO@TiO_2 NRs. (f) The high-resolution XPS spectra of Ni 2p. Inset: The high-resolution XPS spectra of Ba 3d.

Electrochemical Characterization. To acquire more information on the PEC properties of the as-prepared heterojunctions, the chronoamperometric i-t curves were recorded from the stepwise transient photocurrent responses upon the intermittent light irradiation. As shown in Figure 3a, all the composite KBNNO@TiO_2 NRs (x = 0, 0.1, 0.2, 0.3, 0.4) electrodes with varying contents exhibited higher photocurrent density compared with pristine TiO_2 NRs electrode, the results of which also indicated the successful combination of the KBNNO with the TiO_2 NRs. Significantly, the numerical value of the composite electrodes increased with the doping content and reached to maximum of 0.37 mA cm^{-2} (when x = 0.3), which is about 4.9 times as high as that of pristine TiO_2 NRs (0.075 mA cm^{-2}). Moreover, there is no obvious decline under illumination for 4000 s in electrolyte, as shown in Figure S3, indicating the excellent structural and chemical stability of the as-developed KBNNO@TiO_2 NRs electrodes. These properties can be attributed to the following reasons: (1) Essentially, the excitation through bandgap was a charge from the O 2p states at the maximum of valence band (VB) to the Nb 4d states at the minimum of the conduction band (CB) for

KNO. However, for KBNNO, photoelectrons would be excited from the hybridized Ni 3d states and O 2p states to Nb 4d states, leading to the reduction of the bandgap value.[37-38] Therefore, the Ni-doped-KBNNO shell, with appropriate bandgap, could absorb broad light and served as an effective photosensitizer in the heterostructures. (2) The photoelectrons would transfer to the oxygen vacancies states after being excited to Nb 4d states from the hybridized states, followed by transfer to TiO_2 NRs. The experimental phenomenon caused by oxygen vacancies had been presented in Figure S4. Note that the existence of oxygen vacancies in KBNNO was extremely beneficial to lengthen life spans of photoinduced carriers and decrease the recombination of photo electrons and holes.[50, 51] Firstly, the oxygen vacancies states could be inserted between the CB of KBNNO and CB of TiO_2, which could act as capture center to acquire the electrons transferred from CB of KBNNO, inducing the photogenerated electrons prefer to inject into oxygen vacancies states rather than return to the valence band of KBNNO. Secondly, the oxygen vacancy, served as an active electron trap, could effectively delay the recombination of electrons and holes between oxygen vacancies states and the ground state. Thirdly, the lifetimes of photo electrons in electron traps are multiple expansions longer than that in the CB. These characteristics provide a big advantage for reduce the charge recombination losses and allow the fast electron injection into the CB of TiO_2, followed by collected in FTO substrate through the well-aligned crystalline TiO_2 NRs. (3) As an excellent ferroelectric, Ni/Ba-doped KBNNO with inernal fields induced spontaneous polarization band bending, is also beneficial to the spatial separation of photo-generated charge carriers, and thereby reducing the recombination of photo-induced electrons-holes pairs.

Figure 3b presents a set of linear sweep voltammograms (LSV) that were conducted in dark and under light illumination. All the pristine TiO_2 NRs and KBNNO@TiO_2 NRs (x = 0, 0.1, 0.2, 0.3, 0.4) photoelectrodes exhibited low dark current compared with their corresponding photocurrents, manifesting no drastic electrocatalytic water-splitting happens. Apparently, the photocurrent density of KBNNO@TiO_2 NRs photoelectrodes under illumination also increased with the doping content when $x \leq 0.3$ and decreased when x = 0.4, and all the heterojunction photoelectrodes exhibited higher current than that of pristine TiO_2 NRs electrode, which was corresponding to the results of i-t tests. In addition, the onset potential of KBNNO@TiO_2 NRs (x = 0.3) photoelectrode exhibits -0.983 V *vs.* SCE, which appeared a slightly shift compared with -0.886 V *vs.* SCE for pristine TiO_2 NRs. The lower onset potential value would make charge separation and transportation more efficiently in KBNNO@TiO_2 NRs (x = 0.3) photoelectrode. The electrochemical impedance spectroscopy (EIS) was then tested on these photoelectrodes under one light irradiation covering the frequency interval of 10^5 to 10^{-2} Hz with an amplitude of 5 mV. As shown in Figure 3c, obviously, only one semicircle was obtained in the EIS Nyquist plot. However, a larger radius resistance-circle obtained for pure $KNbO_3$@TiO_2 NRs compound than pristine TiO_2 NRs, which was mainly due to low electronic conductivity of $KNbO_3$ material. It was interesting to see that the Ni/Ba-doped KBNNO@TiO_2 NRs photoelectrodes achieved smaller resistance-circles than pristine TiO_2 NRs with the increasing of Ni/Ba content, suggesting the dramatically reducement of the charge-transfer resistance at the electrode/electrolyte interface after deposition of KBNNO shell. In all, with balanced property, the KBNNO@TiO_2 NRs (x = 0.3) was selected for subsequent utilization.

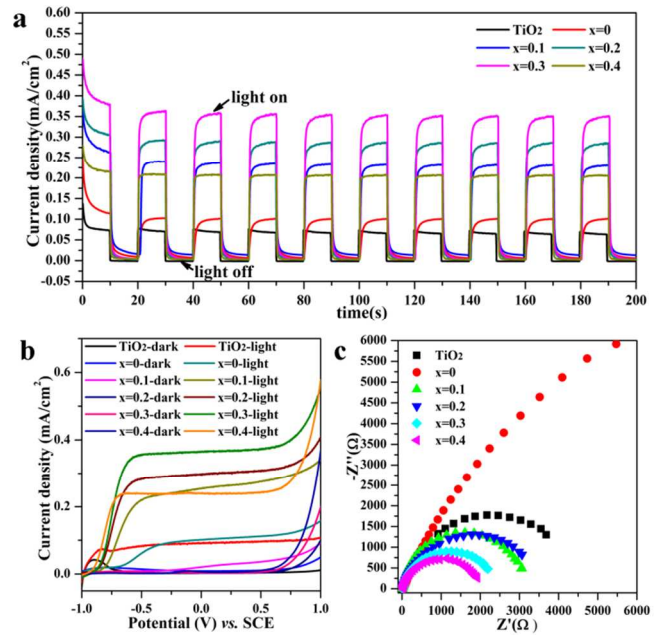

Figure 3. (a) The transient photocurrent responses (i-t) of pristine TiO_2 NRs and KBNNO@TiO_2 NRs (x = 0, 0.1, 0.2, 0.3, 0.4) photoelectrodes at the potential of 0.3 V *vs.* SCE under 100 mW cm^{-2} illumination. (b) The linear sweep voltammograms of pristine TiO_2 NRs and KBNNO@TiO_2 NRs (x = 0, 0.1, 0.2, 0.3, 0.4) photoelectrodes collected in dark and under 100 mW cm^{-2} exposure with scan rate of 0.1 mV s^{-1}. (c) EIS Nyquist of TiO_2 NRs and KBNNO@TiO_2 NRs (x = 0, 0.1, 0.2, 0.3, 0.4) photoelectrodes measured under light irradiation (100 mW cm^{-2}).

PEC detection. The KBNNO@TiO_2 NRs was then applied for the quantitative determination of Cys, an important indicator of many biological processes. Specifically, the responses of the KBNNO@TiO_2 NRs (x = 0.3) electrode to Cys was studied via the time-dependent current measurements at 0.0 V applied voltage. As illustrated in Scheme 1b, the consumption of the photoexcited holes in KBNNO would contribute to efficient photoinduced charge separation and thus lead to the enhancement of photocurrent. In other words, with the increase of Cys concentration, more photoexcited holes on the VB of KBNNO were steered to oxidize Cys, therefore the response of photocurrent was increased correspondingly as observed in Figure 4a and 4b. Figure 4c depicted the corresponding derived calibration curve with a wide linear range from 5.0×10^{-6} to 1.0×10^{-2} M and its detection limit was found as 1.3×10^{-6} mol L^{-1}, which was comparable to those obtained by cyclic voltammetry, colorimetry, amperometry, electrogenerated chemiluminescence (ECL) method and other PEC methods, as shown in Table S1. Since the concentration of Cys in human serum varies from 165.1 to 335.3 μmol L^{-1}, the results indicated the developed system processed great potential for Cys detection in biological applications. The reproducibility of this PEC bioanalysis was then assessed by relative standard deviation (RSD), and the RSD of 6.4% was obtained by

testing three electrodes at the concentration of 1.0×10^{-4} mol L^{-1} independently, suggesting favorable reproducibility.

The selectivity was then evaluated through the detection of some common interferents. Among the common potential interferents in human serum, the thiol-containing biomolecules such as GSH and Hcy, which process the similar structures with Cys, should be considered primarily. Specifically, it was documented that the normal concentration of GSH is at the level of 14.0 ± 7 μmol L−1, which is nearly 10 times lower than the concentration of Cys (165.1-335.3 μmol L^{-1}).[52, 53] Therefore, the interfering GSH was set at the level of 1.0×10^{-5} mol L^{-1} in this selectivity test and no obvious response was produced compared with the responce of Cys. To some extent, it was due to the distinction of electron-donating ability between GSH and Cys, which has provided particular explanation in previous study.[15] Likewise, the discriminability of system to Hcy was investigated. Although Hcy has a very similar structure to cysteine, it is present in a much lower concentration (5-15 μM) than Cys in healthy human serum.[54,55] As a consequence, at the concentration of 1.0×10^{-5} mol L^{-1}, the signal of Hcy was rather low which could hardly impact the performance of the as-fabricated electrode. Besides, considering the normal physiological glucose level in human blood was 3-8 mM, which is nearly 30 times higher than those of many of the interfering species.[56] The level of glucose was chose as 1.0×10^{-2} mol L^{-1}. Other interferences including Lys, Lac, Sar, Try, BSA, DA, AA, UA and Urea were set at the level of 1.0×10^{-3} mol L^{-1} which remained the same concentration with Cys. As shown in Figure 4d, it was demonstrated that none of these interference factors could cause obvious photocurrent response except the target Cys, demonstrating the favorable selectivity of the system.

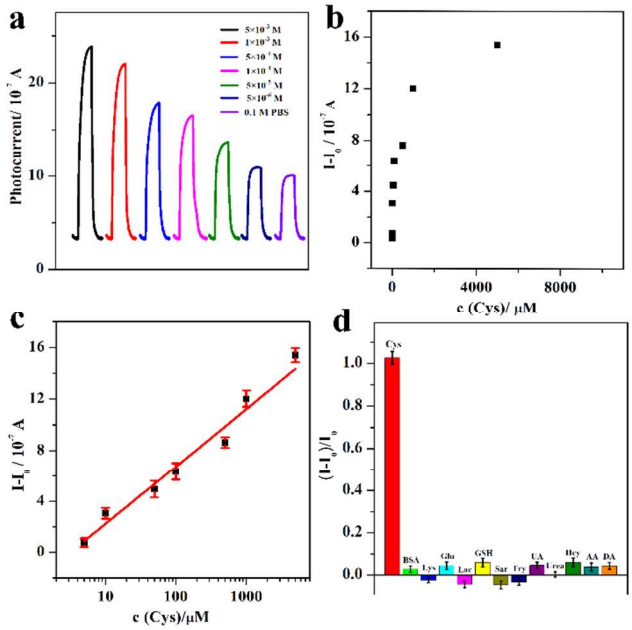

Figure 4. (a) Photocurrent responses of the KBNNO@TiO_2 NRs electrodes with variable Cys concentrations. (b) Plot of the photocurrent vs Cys concentration. (c) The derived calibration curve. (d) Selectivity of the system toward common interference species. I_0 is the photocurrent intensity measured in the PBS solution (0.1 M, pH 7.4), I is the intensity after the addition of Cys and different interfering reagents. The PEC tests were performed with 0.0 V applied voltage (vs. Ag/AgCl).

CONCLUSIONS

In conclusion, this work has explored and exhibited the potential of ferroelectric perovskite oxide-based heterostructures for PEC bioanalytical application. Exemplified by KBNNO@TiO_2 NRs, the sample was prepared by the combined use of solid state synthesis, hydrothermal method and PLD, and then systematically characterized by various techniques, which revealed the desired integration of KBNNO with TiO_2 NRs. As shown in the chronoamperometric *I-t* results, PEC tests also manifested the favorable alignment between the KBNNO and TiO_2 NRs. For the detection of Cys, the PEC sensor demonstrated desirable performance in terms of good sensitivity and stability. These results clearly indicated that the KBNNO@TiO_2 NRs heterojunction could be a competitive candidate platform in the development of PEC bioanalysis. This work not only featured the first use of a unique KBNNO@TiO_2 NRs in PEC bioanalysis but also offered a new perspective for the general development of numerous ferroelectrics-based heterostructure for innovative applications in this field. We further expect the ingenious implementation of these materials would lead to advanced PEC biosensors and devices with superior analytical performance.

ASSOCIATED CONTENT

Supporting Information

EDS mapping of as-prepared KBNNO powder (x = 0.3), SEM images of KBNNO nanoparticles at varying doping content, The photocurrent responses upon light irradiation for 4000 s, Typical decay and rise curve for KBNNO@TiO_2 NRs (x = 0.3) photoelectrode under light off and on, Comparison of Different Methods for L-Cys Determination (PDF).

AUTHOR INFORMATION

Corresponding Author

* E-mail: qupeng0212@163.com

* E-mail: zww@nju.edu.cn; zww@stanford.edu

Author Contributions

L.-M.Y., Y.-C.Z. and Y.-L. L. contributed equally.

Notes

The authors declare no competing financial interest.

ACKNOWLEDGMENT

We thank the National Natural Science Foundation of China (Grant Nos. 21605100, 21505091, 21405103 and 21675080), Henan Joint International Research Laboratory of Chemo/Biosensing and Early Diagnosis of Major Diseases and Natural Science Foundation of Jiangsu Province (Grant BK20170073) for support.

REFERENCES

(1) Tanne, J.; Schäfer, D.; Khalid, W.; Parak, W. J.; Lisdat, F. Light-Controlled Bioelectrochemical Sensor Based on CdSe/ZnS Quantum Dots. *Anal. Chem.* **2011,** *83,* 7778-7785.

(2) Zayats, M.; Kharitonov, A. B.; Pogorelova, S. P.; Lioubashevski, O.; Katz, E.; Willner, I. Probing Photoelectrochemical Processes in Au-CdS Nanoparticle Arrays by Surface Plasmon Resonance: Application for the Detection of Acetylcholine Esterase Inhibitors. *J. Am. Chem. Soc.* **2003,** *125,* 16006-16014.

(3) Zhao, W.-W.; Xu, J.-J.; Chen, H.-Y. Photoelectrochemical DNA Biosensors. *Chem. Rev.* **2014,** *114,* 7421-7441.

(4) Zhao, W.-W.; Xu, J.-J.; Chen, H.-Y. Photoelectrochemical Bioanalysis: the State of the Art. *Chem. Soc. Rev.* **2015,** *44,* 729-741.

(5) Haddour, N.; Chauvin, J.; Gondran, C.; Cosnier, S. Photoelectrochemical Immunosensor for Label-Free Detection and Quantification of Anti-cholera Toxin Antibody. *J. Am. Chem. Soc.* **2006,** *128,* 9693-9698.

(6) Zhao, W.-W.; Xu, J.-J.; Chen, H.-Y. Photoelectrochemical Aptasensing. *TrAC, Trends Anal. Chem.* **2016,** *82,* 307-315.

(7) Tang, J.; Zhang, Y.; Kong, B.; Wang, Y.; Da, P.; Li, J.; Elzatahry, A. A.; Zhao, D.; Gong, X.; Zheng, G. Solar-Driven Photoelectrochemical Probing of Nanodot/Nanowire/Cell Interface. *Nano Lett.* **2014,** *14,* 2702-2708.

(8) Hao, N.; Zhang, Y.; Zhong, H.; Zhou, Z.; Hua, R.; Qian, J.; Liu, Q.; Li, H.; Wang, K. Design of a Dual Channel Self-Reference Photoelectrochemical Biosensor. *Anal. Chem.* **2017,** *89,* 10133-10136.

(9) Mei, L.-P.; Liu, F.; Pan, J.-B.; Zhao, W.-W.; Xu, J.-J.; Chen, H.-Y. Enediol-Ligands-Encapsulated Liposomes Enables Sensitive Immunoassay: A Proof-of-Concept for General Liposomes-Based Photoelectrochemical Bioanalysis. *Anal. Chem.* **2017,** *89,* 6300-6304.

(10) Guo, L.; Li, Z.; Marcus, K.; Navarro, S.; Liang, K.; Zhou, L.; Mani, P.; Florczyk, S.; Coffey, K.; Orlovskaya, N.; Sohn, Y.; Yang, Y. Periodically Patterned Au-TiO_2 Heterostructures for Photoelectrochemical Sensor. *ACS Sens.* **2017,** *2,* 621-625.

(11) Zhao, W.-W.; Yu, X.-D.; Xu, J.-J.; Chen, H.-Y. Recent Advances in the Use of Quantum Dots for Photoelectrochemical Bioanalysis. *Nanoscale* **2016,** *8,* 17407-17414.

(12) Yan, K.; Liu, Y.; Yang, Y.; Zhang, J. A Cathodic "Signal-off" Photoelectrochemical Aptasensor for Ultrasensitive and Selective Detection of Oxytetracycline. *Anal. Chem.* **2015,** *87,* 12215-12220.

(13) Zhu, Y.-C.; Zhang, N.; Ruan, Y.-F.; Zhao, W.-W.; Xu, J.-J.; Chen, H.-Y. Alkaline Phosphatase Tagged Antibodies on Gold Nanoparticles/TiO_2 Nanotubes Electrode: A Plasmonic Strategy for Label-Free and Amplified Photoelectrochemical Immunoassay. *Anal. Chem.* **2016,** *88,* 5626-5630.

(14) Zhao, W.-W.; Ma, Z.-Y.; Yu, P.-P.; Dong, X.-Y.; Xu, J.-J.; Chen, H.-Y. Highly Sensitive Photoelectrochemical Immunoassay with Enhanced Amplification Using Horseradish Peroxidase Induced Biocatalytic Precipitation on a CdS Quantum Dots Multilayer Electrode. *Anal. Chem.* **2012,** *84,* 917-923.

(15) Long, Y. T.; Kong, C.; Li, D. W.; Li, Y.; Chowdhury, S.; Tian, H. Ultrasensitive Determination of Cysteine Based on the Photocurrent of Nafion-Functionalized CdS-MV Quantum Dots on an ITO Electrode. *Small* **2011,** *7,* 1624-1628.

(16) Li, H.; Mu, Y.; Yan, J.; Cui, D.; Ou, W.; Wan, Y.; Liu, S. Label-Free Photoelectrochemical Immunosensor for Neutrophil Gelatinase-Associated Lipocalin Based on the Use of Nanobodies. *Anal. Chem.* **2015,** *87,* 2007-2015.

(17) Li, X.; Zhu, L.; Zhou, Y.; Yin, H.; Ai, S. Enhanced Photoelectrochemical Method for Sensitive Detection of Protein Kinase A Activity Using TiO_2/g-C_3N_4, PAMAM Dendrimer, and Alkaline Phosphatase. *Anal. Chem.* **2017,** *89,* 2369-2376.

(18) Li, C.; Lu, W.; Zhu, M.; Tang, B. Development of Visible-Light Induced Photoelectrochemical Platform Based on Cyclometalated Iridium(III) Complex for Bioanalysis. *Anal. Chem.* **2017,** *89,* 11098-11106.

(19) Shu, J.; Qiu, Z.; Lin, Z.; Cai, G.; Yang, H.; Tang, D. Semiautomated Support Photoelectrochemical Immunosensing Platform for Portable and High-Throughput Immunoassay Based on Au Nanocrystal Decorated Specific Crystal Facets $BiVO_4$ Photoanode. *Anal. Chem.* **2016,** *88,* 12539-12546.

(20) Wang, G.-L.; Yuan, F.; Gu, T.; Dong, Y.; Wang, Q.; Zhao, W.-W. Enzyme-Initiated Quinone-Chitosan Conjugation Chemistry: Toward A General in Situ Strategy for High-Throughput Photoelectrochemical Enzymatic Bioanalysis. *Anal. Chem.* **2018,** *90,* 1492-1497.

(21) Li, R.; Zhang, Y.; Tu, W.; Dai, Z. Photoelectrochemical Bioanalysis Platform for Cells Monitoring Based on Dual Signal Amplification Using in Situ Generation of Electron Acceptor Coupled with Heterojunction. *ACS Appl. Mat. Interfaces* **2017,** *9,* 22289-22297.

(22) Zhang, N.; Ruan, Y.-F.; Ma, Z.-Y.; Zhao, W.-W.; Xu, J.-J.; Chen, H.-Y. Simultaneous Photoelectrochemical and Visualized Immunoassay of β-human Chorionic Gonadotrophin. *Biosens. Bioelectron.* **2016,** *85,* 294-299.

(23) Ma, Z.-Y.; Xu, F.; Qin, Y.; Zhao, W.-W.; Xu, J.-J.; Chen, H.-Y. Invoking Direct Exciton–Plasmon Interactions by Catalytic Ag Deposition on Au Nanoparticles: Photoelectrochemical Bioanalysis with High Efficiency. *Anal. Chem.* **2016,** *88,* 4183-4187.

(24) Lan, F.; Sun, G.; Liang, L.; Ge, S.; Yan, M.; Yu, J. Microfluidic Paper-Based Analytical Device for Photoelectrochemical Immunoassay with Multiplex Signal Amplification Using Multibranched Hybridization Chain Reaction and PdAu Enzyme Mimetics. *Biosens. Bioelectron.* **2016,** *79,* 416-422.

(25) Pang, X.; Bian, H.; Su, M.; Ren, Y.; Qi, J.; Ma, H.; Wu, D.; Hu, L.; Du, B.; Wei, Q. Photoelectrochemical Cytosensing of RAW264.7 Macrophage Cells Based on a TiO_2 Nanoneedls@MoO_3 Array. *Anal. Chem.* **2017,** *89,* 7950-7957.

(26) Zhao, W.-W.; Zhang, L.; Xu, J.-J.; Chen, H.-Y. Cell Surface Carbohydrates Evaluation via a Photoelectrochemical Approach. *Chem. Commun.* **2012,** *48,* 9456-9458.

(27) Kang, Z.; Yan, X.; Wang, Y.; Zhao, Y.; Bai, Z.; Liu, Y.; Zhao, K.; Cao, S.; Zhang, Y. Self-Powered Photoelectrochemical Biosensing Platform based on Au NPs@ZnO Nanorods Array. *Nano Research* **2016,** *9,* 344-352.

(28) Li, R.; Liu, Y.; Yan, T.; Li, Y.; Cao, W.; Wei, Q.; Du, B. A Competitive Photoelectrochemical Assay for Estradiol based on in situ Generated CdS-enhanced TiO_2. *Biosens. Bioelectron.* **2015,** *66,* 596-602.

(29) Zhao, W.-W.; Xu, J.-J.; Chen, H.-Y. Photoelectrochemical Enzymatic Biosensors. *Biosens. Bioelectron.* **2017,** *92,* 294-304.

(30) Zhao, W.-W.; Xu, J.-J.; Chen, H.-Y. Photoelectrochemical Immunoassays. *Anal. Chem.* **2018,** *90,* 615-627.

(31) Liu, Y.; Yan, K.; Zhang, J. Graphitic Carbon Nitride Sensitized with CdS Quantum Dots for Visible-Light-Driven Photoelectrochemical Aptasensing of Tetracycline. *ACS Appl. Mat. Interfaces* **2016,** *8,* 28255-28264.

(32) Qiu, Z.; Shu, J.; Tang, D. Near-Infrared-to-Ultraviolet Light-Mediated Photoelectrochemical Aptasensing Platform for Cancer Biomarker Based on Core–Shell $NaYF_4$:Yb,Tm@TiO_2 Upconversion Microrods. *Anal. Chem.* **2018,** *90,* 1021-1028.

(33) Ruan, Y.-F.; Zhang, N.; Zhu, Y.-C.; Zhao, W.-W.; Xu, J.-J.; Chen, H.-Y. Photoelectrochemical Bioanalysis Platform of Gold Nanoparticles Equipped Perovskite Bi_4NbO_8Cl. *Anal. Chem.* **2017,** *89,* 7869-7875.

(34) Nechache, R.; Harnagea, C.; Li, S.; Cardenas, L.; Huang, W.; Chakrabartty, J.; Rosei, F. Bandgap Tuning of Multiferroic Oxide Solar Cells. *Nat. Photonics* **2014,** *9,* 61-67.

(35) Morris, M. R.; Pendlebury, S. R.; Hong, J.; Dunn, S.; Durrant, J. R. Effect of Internal Electric Fields on Charge Carrier Dynamics in a Ferroelectric Material for Solar Energy Conversion. *Adv. Mater.* **2016,** *28,* 7123-7128.

(36) Yang, S. Y.; Martin, L. W.; Byrnes, S. J.; Conry, T. E.; Basu, S. R.; Paran, D.; Reichertz, L.; Ihlefeld, J.; Adamo, C.; Melville, A. Photovoltaic Effects in $BiFeO_3$. *Appl. Phys. Lett.* **2009,** *95,* 062909.

(37) Grinberg, I.; West, D. V.; Torres, M.; Gou, G.; Stein, D. M.; Wu, L.; Chen, G.; Gallo, E. M.; Akbashev, A. R.; Davies, P. K.; Spanier, J. E.; Rappe, A. M. Perovskite Oxides for Visible-light-absorbing Ferroelectric and Photovoltaic Materials. *Nature* **2013,** *503,* 509-512.

(38) Zhou, W.; Deng, H.; Yang, P.; Chu, J. Structural Phase Transition, Narrow Band Gap, and Room-Temperature Ferromagnetism in $[KNbO_3]_{1-x}[BaNi_{1/2}Nb_{1/2}O_{3-\delta}]_x$ Ferroelectrics. *Appl. Phys. Lett.* **2014,** *105,* 111904.

(39) Wu, P.; Wang, G.; Chen, R.; Guo, Y.; Ma, X.; Jiang, D. Enhanced Visible Light Absorption and Photocatalytic Activity of $[KNbO_3]_{1-x}[BaNi_{0.5}Nb_{0.5}O_{3-\delta}]_x$ Synthesized by Sol–Gel based Pechini method. *RSC Adv.* **2016,** *6,* 82409-82416.

(40) Lombardi, J.; Pearsall, F.; Li, W.; O'Brien, S. Synthesis and Dielectric Properties of Nanocrystalline Oxide Perovskites, $[KNbO_3]_{1-x}[BaNi_{0.5}Nb_{0.5}O_{3-\delta}]_x$, Derived from Potassium Niobate $KNbO_3$ by Gel Collection. *J. Mater. Chem. C* **2016,** *4,* 7989-7998.

(41) Zhang, T.; Zhao, K.; Yu, J.; Jin, J.; Qi, Y.; Li, H.; Hou, X.; Liu, G. Photocatalytic Water Splitting for Hydrogen Generation on Cubic, Orthorhombic, and Tetragonal $KNbO_3$ Microcubes. *Nanoscale* **2013,** *5,* 8375-8383.

(42) Yu, L.; Jia, J.; Yi, G.; Yu, S.; Han, M. Bandgap Tuning of $[KNbO_3]_{1-x}[BaCo_{1/2}Nb_{1/2}O_{3-\delta}]_x$ Ferroelectrics. *Mater. Lett.* **2016,** *184,* 166-168.

(43) Yu, L.; Jia, J.; Yi, G. A New-Type Inorganic $[KNbO_3]_{0.9}[BaCo_{1/2}Nb_{1/2}O_{3-\delta}]_{0.1}$ Perovskite Oxide as Sensitizer for Photovoltaic Cell. *Physica Status Solidi* **2017,** *214,* 1600540.

(44) Liu, B. Oriented Single-Crystalline Rutile TiO_2 Nanorods on Transparent Conducting Substrates for Dye-Sensitized Solar Cells. *J. Am. Chem. Soc.* **2009,** *131,* 3985-3990.

(45) Berhe, S. A.; Nag, S.; Molinets, Z.; Youngblood, W. J. Influence of Seeding and Bath Conditions in Hydrothermal Growth of Very Thin (~20 nm) Single-Crystalline Rutile TiO_2 Nanorod Films. *ACS Appl. Mat. Interfaces* **2013,** *5,* 1181-1185.

(46) Bansode, U.; Naphade, R.; Game, O.; Agarkar, S.; Ogale, S. Hybrid Perovskite Films by a New Variant of Pulsed Excimer Laser Deposition: A Room-Temperature Dry Process. *J. Phys. Chem. C* **2015,** *119,* 9177-9185.

(47) Choi, W. S.; Rouleau, C. M.; Seo, S. S. A.; Luo, Z.; Zhou, H.; Fister, T. T.; Eastman, J. A.; Fuoss, P. H.; Fong, D. D.; Tischler, J. Z. Atomic Layer Engineering of Perovskite Oxides for Chemically Sharp Heterointerfaces. *Adv. Mater.* **2012,** *24,* 6423-6428.

(48) Rani, J.; Yadav, K. L.; Prakash, S. Modified Structure and Electrical Properties of BSZT Doped KNN Hybrid Ceramic. *Appl. Phys. A* **2012,** *108,* 761-764.

(49) Luisman, L.; Feteira, A.; Reichmann, K. Weak-Relaxor Behaviour in Bi/Yb-doped $KNbO_3$ Ceramics. *Appl. Phys. Lett.* **2011,** *99,* 192901.

(50) Xu, L.; Li, X.; Zhan, Z.; Wang, L.; Feng, S.; Chai, X.; Lu, W.; Shen, J.; Weng, Z.; Sun, J. Catalyst-Free, Selective Growth of ZnO Nanowires on SiO_2 by Chemical Vapor Deposition for Transfer-Free Fabrication of UV Photodetectors. *ACS Appl. Mat. Interfaces* **2015,** *7,* 20264-20271.

(51) Nakamura, I.; Negishi, N.; Kutsuna, S.; Ihara, T.; Sugihara, S.; Takeuchi, K. Role of Oxygen Vacancy in the Plasma-Treated TiO_2 Photocatalyst with Visible Light Activity for NO Removal. *J. Mol. Catal. A: Chem.* **2000,** *161,* 205-212.

(52) Jacobsen, D.-W.; Gatautis, V.-J.; Green, R.; Robinson, K.; Savon, S. R.; Secic, M.; Ji, J.; Otto, J. M.; Taylor, L. M. Rapid HPLC Determination of Total Homocysteine and other Thiols in Serum and Plasma: Sex Differences and Correlation with Cobalamin and Folate Concentrations in Healthy Subjects. *Clin. Chem.* **1994,** *40,* 873-881.

(53) Yang, X.-F.; Huang, Q.; Zhong, Y.; Li, Z.; Li, H.; Lowry, M.; Escobedo, J. O.; Strongin, R. M. A dual Emission Fluorescent Probe Enables Simultaneous Detection of Glutathione and Cysteine/Homocysteine. *Chem. Sci.* **2014,** *5,* 2177-2183.

(54) Zhang, Y.; Li, Y.; Yan, X.-P. Photoactivated CdTe/CdSe Quantum Dots as a Near Infrared Fluorescent Probe for Detecting Biothiols in Biological Fluids. *Anal. Chem.* **2009**, *81*, 5001-5007.

(55) Qian, Q.; Deng, J.; Wang, D.; Yang, L.; Yu, P.; Mao, L. Aspartic Acid-Promoted Highly Selective and Sensitive Colorimetric Sensing of Cysteine in Rat Brain. *Anal. Chem.* **2012**, *84*, 9579-9584.

(56) Dai, W.-X.; Zhang, L.; Zhao, W.-W.; Yu, X.-D.; Xu, J.-J.; Chen, H.-Y. Hybrid PbS Quantum Dot/Nanoporous NiO Film Nanostructure: Preparation, Characterization, and Application for a Self-Powered Cathodic Photoelectrochemical Biosensor. *Anal. Chem.* **2017,** *89,* 8070-8078.

For TOC only